PHOTONICS Research

Monitoring and identifying pendant droplets in microbottle resonators

Zijie Wang, Xiaobei Zhang,* Qi Zhang, Yiqi Chen, Yong Yang, Yang Yu, Yang Wang, Yanhua Dong, Yi Huang, and Tingyun Wang

Key Laboratory of Specialty Fiber Optics and Optical Access Networks, Joint International Research Laboratory of Specialty Fiber Optics and Advanced Communication, Shanghai Institute for Advanced Communication and Data Science, Shanghai University, Shanghai 200444, China
**Corresponding author: xbzhang@shu.edu.cn*

Received 7 December 2021; revised 30 December 2021; accepted 31 December 2021; posted 4 January 2022 (Doc. ID 450535); published 22 February 2022

Optofluidic resonators are capable of characterizing various fluidic media. Here, we propose an optofluidic microbottle resonator (OFMBR) that is applied to generate pendant droplets, whose maximum mass is related to the liquid surface tension. Mass and type of droplets forming along the OFMBR stem can be monitored in real time by spectrum variation. As a pendant droplet grows, increased droplet gravity introduces a decreased coupling gap and compressive force between the tapered fiber and OFMBR, leading to a resonance wavelength shift. The operation mechanism of the proposed sensors is validated by theoretical simulation and experimental results. From the experimental spectra, a liquid mass sensor with maximum sensitivity of −3.34 pm/mg is obtained, and distilled water and alcohol can be identified. This scheme provides a new thread for droplet generation as well as fluidic properties characterization.

https://doi.org/10.1364/PRJ.450535

1. INTRODUCTION

Manipulating microvolume droplet and characterizing droplet properties are of great importance in life science and biological applications, e.g., drug discovery, particle sorting, droplet generation [1–3]. Droplet properties have been extensively investigated in the past years, including effective surface tension and viscosity, dynamic evaporation, and droplet oscillation, etc. [4–6]. Specifically, a droplet can function as a resonator to excite the whispering gallery mode (WGM), owing to its smooth surface and spherical morphology [7–9]. It provides an excellent platform to investigate optomechanics, by virtue of the characteristic of being hundreds of times softer than solid resonators [10]. Accordingly, the deformation of droplets driven by photon pressure can be determined [10,11]. Actually, the above-mentioned investigations rely on auxiliary devices to sustain the morphology of droplets, such as solid substrates and optical fiber end face and stem [10–12]. In addition, the specific technologies and high-speed cameras are necessary to manipulate droplet position and capture motion images [13,14].

Optofluidic capillary is a promising candidate to characterize the fluid properties due to the inherently fluidic channel [15,16]. Recently, WGMs in a microcapillary-based droplet resonator have been demonstrated to measure droplet morphologic variation with nanoscale precision [17]. Compared with a microcapillary, an optofluidic microbottle resonator (OFMBR) can enhance light–matter interaction, thanks to well-confined WGMs [18–20]. It has attracted enormous attention in microfluidic application, including gas and gas concentration identification [21,22], magnetic field intensity and bimolecular binding event monitoring [23–25], and ultrasound and nanoparticle detection [26–29]. Furthermore, monitoring of dynamic flow rates and the phase transition of hydrogel are demonstrated [30–33]. However, there are few demonstrations, to the best of our knowledge, in which OFMBR is employed to characterize liquid properties and identify liquid types.

Herein, monitoring liquid mass and radius in real time and identifying liquid types in OFMBR are demonstrated by observing resonance wavelength variation. Thanks to liquid surface tension and solid–liquid interfacial forces, liquid outflowing from an OFMBR end face forms a pendant droplet along its stem. The growing droplet gravity decreases the coupling gap and introduces compressive force between the tapered fiber and OFMBR, which shifts the resonance wavelength. Theoretically, the displacement on OFMBR caused by droplet gravity is simulated using COMSOL simulation software, which is based on solving a Navier equation. Liquid mass and liquid identification experiments are carried out, and the morphology of a pendant droplet is monitored by a CCD camera. Our scheme paves the way for applications of droplet generation and liquid properties characterization.

2. OPERATION PRINCIPLE AND THEORETICAL ANALYSIS

The schematic diagram of the proposed sensor is shown in Fig. 1(a), which utilizes a tapered fiber perpendicularly coupling with a horizontally placed OFMBR. One end of the OFMBR connects to a commercial syringe pump to inject fluid with controllable and stable flow rates. The other flat end face is kept open to serve as a pendant droplet generator. The liquid outflowing from the OFMBR end face forms a pendant droplet along its stem thanks to the liquid surface tension and solid–liquid interfacial forces. Further, the pendant droplet will detach from the stem when the growing droplet gravity is greater than the liquid surface tension.

The schematic of spectrum variations during pendant droplet formation, as illustrated in Fig. 1(b), can be clarified in three stages. In the first stage, the coupling gap between the OFMBR and tapered fiber maintains beyond the coupling region. In consequence, the WGM will not be excited, presenting a flat transmission spectrum. After that, the liquid outflowing from the OFMBR end face starts to form a pendant droplet along its stem. In the second stage, the growing gravity of the pendant droplet decreases the coupling gap, prompting to excite the WGM. In the third stage, the persistently growing gravity results in the physical contact and compressive force between tapered fiber and OFMBR. The compressive force then introduces a decreased radius of OFMBR, resulting in a blue-shift of the resonance wavelength with a decreasing signal intensity. The maximum wavelength shift can be obtained when the droplet gravity is equal to liquid surface tension. Subsequently, the pendant droplet detaches from the stem, a new pendant droplet forms, and the above-mentioned stages repeat simultaneously.

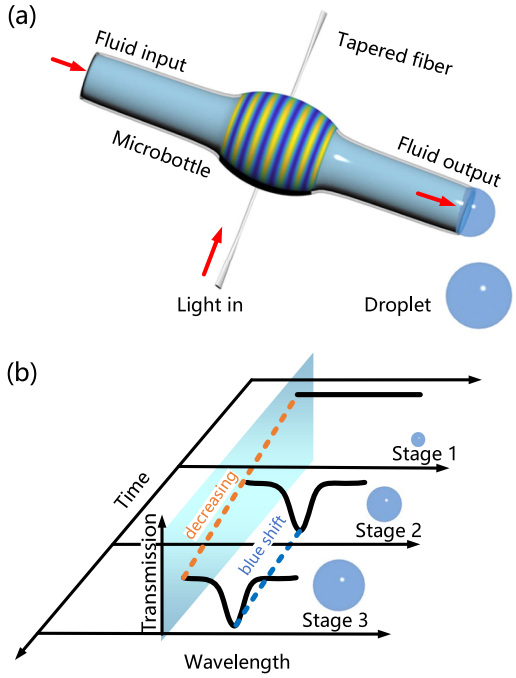

Fig. 1. (a) Schematic diagram of the proposed sensor. (b) Spectrum changes under three stages. Blue and orange dashed lines represent variations of the resonance wavelength and signal intensity with time, respectively.

The mass of the pendant droplet can be calculated by multiplying the fluid density by the fluid volume. The radius of the pendant droplet can be deduced according to the sphere volume formula, providing that the morphology of the pendant droplet is approximated as a sphere under microgravity [5,11]. Consequently, the mass and radius of the pendant droplet can be obtained from

$$m = \rho_{\mathrm{dro}} v t, \tag{1}$$

$$r = \left(\frac{3vt}{4\pi}\right)^{\frac{1}{3}}, \tag{2}$$

where m, ρ_{dro}, and r are the mass, density, and radius of the pendant droplet, and terms v and t are the flow rate inside the OFMBR (unit, μL/min) and flow time, respectively.

The operation principle of the proposed sensor is that the gravity of pendant droplet would alter both the refractive index and radius of OFMBR by mechanical and strain effect, respectively. Both variations prompt the resonance wavelength to shift, which can be expressed as

$$\frac{\mathrm{d}\lambda}{\lambda} = \frac{\mathrm{d}R}{R} + \frac{\mathrm{d}n}{n}, \tag{3}$$

where R denotes the maximum outer radius of OFMBR, and n denotes the effective refractive index of resonant mode. Equation (3) reveals that the resonance wavelength shifts toward shorter wavelengths with decreasing R and n. However, the strain effect induced a morphology change that dominates the mechanical effect induced refractive index change [34]. The governing equation for elastic mechanics study is based on equilibrium differential equation, which can be written as

$$\rho_{\mathrm{med}} \frac{\partial^2 \mathbf{u}}{\partial t^2} + d_a \frac{\partial \mathbf{u}}{\partial t} - \nabla \cdot \boldsymbol{\sigma} = \mathbf{f}, \tag{4}$$

where ρ_{med} and d_a are the density of the elastic medium and damping coefficient, and $\mathbf{u}$, $\boldsymbol{\sigma}$, and $\mathbf{f}$ are the displacement vector, stress tensor, and body force vector, respectively. Specifically, the terms on the left-hand of Eq. (4) denote the inertial force, damping force, and stress, where the first two terms can be eliminated when the system is in a steady state [35]. The term on the right-hand of Eq. (4) denotes the body force. Furthermore, Eq. (4) can evolve into a Navier equation by taking account of the geometric and physical equations [36]. It describes the deformation of a continuous, isotropic, and linear elastic medium in the absence of body force [34,37]:

$$(\mu + G)\nabla\nabla \cdot \mathbf{u} + G\nabla^2 \mathbf{u} = 0, \tag{5}$$

where μ and G are Lame constants, which relate to Young's modulus and Poisson's ratio of material. The morphologic variation causing a wavelength shift of the resonator has been systematically investigated in Ref. [34], which reveals that the resonance wavelength dependence on force is essentially linear.

In order to analyze the influence of droplet gravity on device displacement, the solid mechanics interface of COMSOL Multiphysics is employed. As shown in the inset on the top

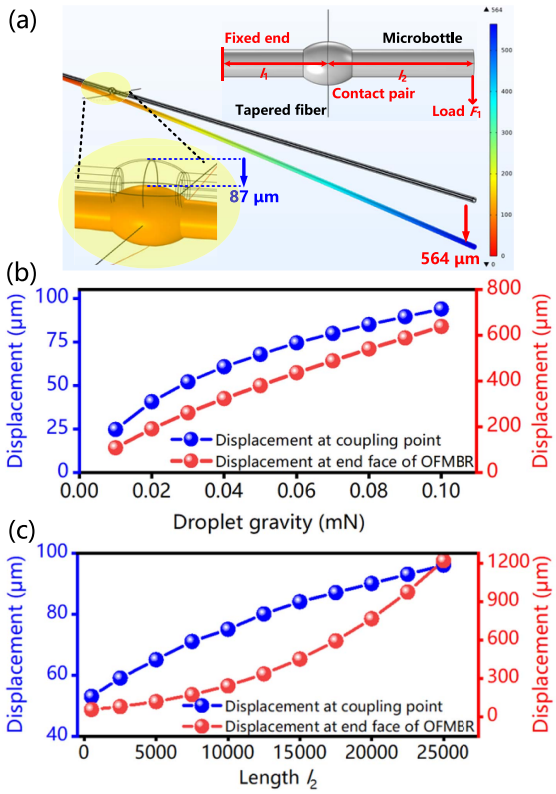

Fig. 2. (a) Simulation result of displacement under droplet gravity when the length l_1 is 13,000 μm and l_2 is 17,000 μm. Inset on top right shows the established model in COMSOL; inset on bottom left is the enlarged view at the coupling point. (b) Influence of droplet gravity on device displacement when l_2 is 17,000 μm. (c) Influence of length l_2 on device displacement when droplet gravity is 0.085 mN.

right of Fig. 2, the simulation model is established, and three boundary conditions are considered: 1) one end of OFMBR and both ends of the tapered fiber are set as fixed ends, where no displacement occurs; 2) a contact pair is established between the OFMBR and tapered fiber; 3) a point load is added at the other end face of OFMBR to simulate the droplet gravity. The terms l_1 and l_2 represent the length from the fixed end of the OFMBR to the coupling point and from the coupling point to the load, respectively. F_1 indicates the load gravity. In the simulation, the OFMBR material properties, including Young's modulus, Poisson's ratio, and material density, are set as 73 GPa, 0.17, and 2200 kg/m^3, respectively. The maximum outer diameter and wall thickness of OFMBR are set as 200 and 8 μm, respectively. The parameter of l_1 is set as the constant of 13,000 μm.

Figure 2(a) shows the simulation result as l_2 and F_1 are set as 17,000 μm and 0.085 mN, whose values are close to reality. It shows that 87 and 564 μm displacements occur at the coupling point and OFMBR end face under the gravity F_1, respectively. Figure 2(b) shows the displacement dependence on the droplet gravity when l_2 is 17,000 μm, where the displacements at both locations increase monotonically with growing droplet gravity. In addition, the value of l_2 can be tailored by cutting it at desired length. Simulations are conducted as l_2 changes from 500 to 25,000 μm by fixed F_1 as 0.085 mN; the obtained result is shown in Fig. 2(c). We note that the displacements simulated here refer to the displacement in the direction of load gravity. The simulation results convey two insights. The first is that the occurring displacement validates the existence of compressive force at the coupling point, which deforms the OFMBR. The second is that the longer l_2 gives rise to the larger displacement at the OFMBR end face. However, a pronounced elastic force is generated when the pendant droplet detaches, which will result in OFMBR vibration and potential coupling position variation. Therefore, the OFMBR with overlong l_2 is not favorable for a stable experiment.

3. EXPERIMENT RESULTS

The OFMBR used in the experiment has a maximum outer diameter of 200 μm and a wall thickness of around 8 μm, which is fabricated by discharging a silica capillary with an inner and outer diameter of 75 and 125 μm (Polymicro, TSP075150), respectively. The microscope image of OFMBR is shown in the dashed box in Fig. 3. The WGMs of OFMBR are evanescently excited by an adiabatic tapered fiber with a diameter of 1 to 2 μm, which is fabricated by a heat-and-pull method and encapsulated in a U-shaped groove to enhance the tapered fiber robustness.

Figure 3 shows the setup for sensing experiments. The light emitted from a tunable semiconductor laser (Santec, TSL-710) at the 1540 nm wavelength band transmits into tapered fiber through a polarization controller (PC) to excite the WGMs of OFMBR. The output light is composed of light propagating directly from tapered fiber and coupling back from the OFMBR, which will be detected by an oscilloscope after a photodetector (PD). The coupling position between the tapered fiber and OFMBR is adjusted by two 3D translation stages via a CCD-assisted *in situ* monitoring system, and the PC is adopted to adjust the polarization state of input light to optimize the WGM spectrum. Additionally, a triangular wave signal generated by a function generator is utilized to drive TSL scanning in a narrow wavelength range; the power of the TSL is set as 0.1 mW to avoid the thermal effect [38]. To avoid external environmental changes induced spectrum shift, the whole setups are placed on an optical air floating

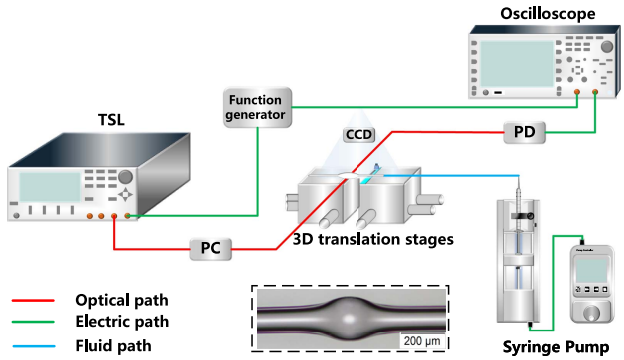

Fig. 3. Schematic diagram of liquid mass and liquid identification sensing system. Inset in the dashed box shows the microscopic image of the OFMBR. TSL, tunable semiconductor laser; CCD, charge coupled device; PD, photodetector; PC, polarization controller.

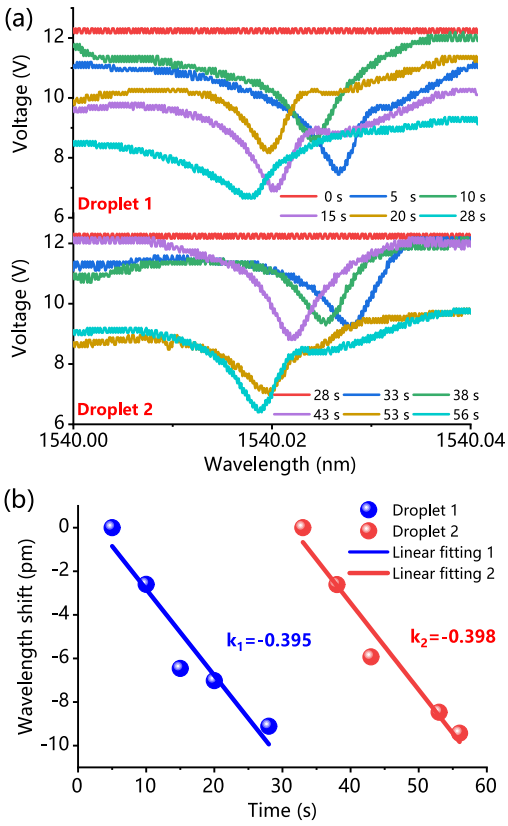

Fig. 4. (a) Resonance wavelength of two pendant droplet changes with flow time as the flow rate of the syringe pump is set as 20 μL/min. (b) Dependence of resonance wavelength shifts on flow time. Dots in the figure represent experiment data; the lines are fitting lines.

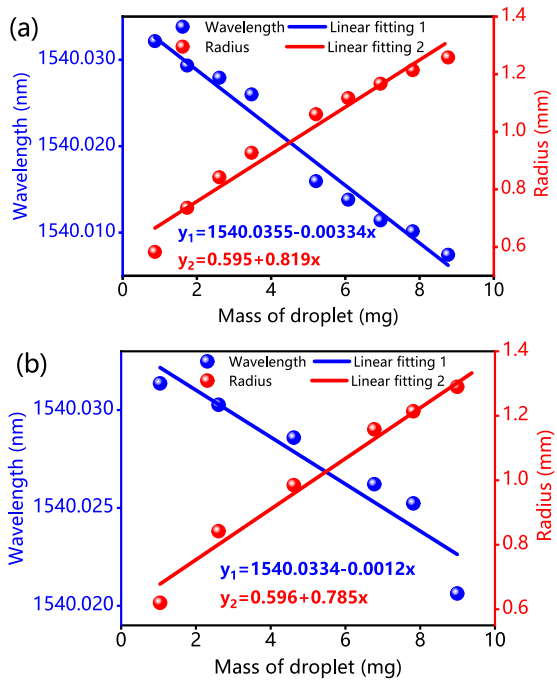

Fig. 5. Resonance wavelength dependence and radius of pendant droplet dependence on droplet mass as the flow rates are (a) 10 μL/min and (b) 30 μL/min.

platform, and the coupling system is protected in an isolated glass box.

In the experiment, we first verify the proposed sensor works with periodicity. We choose a phosphate buffer solution (PBS) with a density of 1.04 g/cm^3 as the fluid material here due to its extensive usage as solvent material in biochemical solutions. The flow rate of the syringe pump is set as 20 μL/min. To observe the influence of droplet gravity on the transmission spectrum comprehensively, the distance of the coupling gap between the OFMBR and tapered fiber is manually adjusted to beyond the coupling region of 3 μm through translation stages, which is favorable for distinguishing Stage 1 and Stage 2, as shown in Fig. 1(b). Therefore, the transmission spectrum only presents a flat line, as indicated by the red line in Fig. 4(a). A visible pendant droplet forms along the OFMBR stem after the syringe pump starts to work due to the surface tension and interfacial forces. Figure 4(a) records the spectrum variations induced by the evolutions of two pendant droplets. The growth of droplet gravity prompts to excite the WGMs and then shifts the resonance wavelength to a shorter wavelength with decreased signal intensity, which is in accordance with our theoretical analysis. The signal intensity fluctuation of dips arises from the coupling position instability as a droplet evolves. Furthermore, the duration of a pendant droplet from generation to detachment is 28 s. As one period completes when a pendant droplet detaches, new pendant droplets form simultaneously, and the spectrum will return to initial state as well. The relationship between resonance wavelength shift and flow time is plotted in Fig. 4(b). It reveals that the maximum wavelength shifts for two pendant droplets are 8.8 and 9.1 pm, which are basically consistent. Moreover, the slopes corresponding to two linear fitting lines are −0.395 and −0.398, indicating the close variation rate of wavelength shift with droplet mass.

In the mass sensing experiment, the PBS is infused into the OFMBR with the stable flow rates of 10 and 30 μL/min. The procedure for the sensing experiment is the same as above, with the obtained results shown in Fig. 5. The detached times of a pendant droplet under 10 and 30 μL/min are around 50 s and 17 s. Accordingly, the maximum pendant droplet mass and radii under two flow rates are 8.77 mg and 1.28 mm, 8.99 mg and 1.29 mm, respectively. The little difference in maximum pendant droplet mass could arise from the difference in formation rates and low time recording accuracy. The resonance wavelength dependence on pendant droplet mass is shown in Figs. 5(a) and 5(b). The obtained sensitivities are −3.34 pm/mg and −1.20 pm/mg at flow rates of 10 and 30 μL/min, respectively. The sensitivity difference could be related to the fact that the overhigh flow rate inside the OFMBR would accelerate the formation rate of the pendant droplet, which induces the OFMBR oscillation as well as instability of the coupling states. The red dots and fitting lines in Figs. 5(a) and 5(b) indicate the relationships between droplet mass and radius, which reveal that the maximum pendant droplet radius is millimeter-scale in our system. To broaden the sensing range of droplet mass, one would employ a capillary with a larger outer diameter and choose liquids with a greater surface tension coefficient.

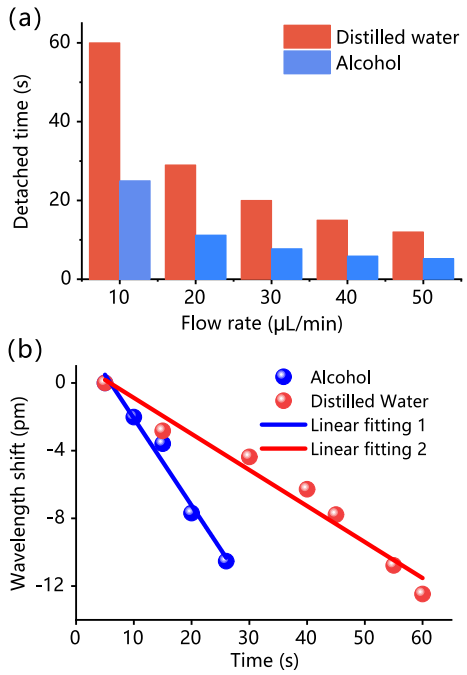

Fig. 6. (a) Detached time for distilled water and alcohol at different flow rates. (b) Dependence of wavelength shift on flow time for distilled water and alcohol.

The proposed structure is also capable of identifying liquids with different surface tension coefficients. The principle is that the larger the surface tension coefficient, the greater the maximum pendant droplet gravity, thus inducing a larger maximum wavelength shift. Distilled water and alcohol are chosen as the detected liquids here owing to their distinguished surface tension coefficients (72.01×10^{-3} N/m for distilled water; 22.3×10^{-3} N/m for alcohol at room temperature). We record the detached time for both liquids at different flow rates, with the result shown in Fig. 6(a), which manifests that the liquid with a larger surface tension coefficient has a longer formation time, corresponding to a bigger droplet gravity. The detached times for distilled water and alcohol at a flow rate of 10 μL/min are around 60 s and 26 s, enabling us to deduce that the maximum droplet masses are around 10 and 3.42 mg, and the maximum radii are 1.34 and 0.95 mm, respectively.

In the liquid identifying experiment, two types of liquids are infused into an individual injection syringe. Then, distilled water passes through the OFMBR with a stable flow rate of 10 μL/min, and a spectrum is recorded as the pendant droplet evolves. Subsequently, the experiment is repeated by employing the other injection syringes filled with alcohol. The wavelength shift dependence on flow time for both liquids is shown in Fig. 6(b), which reveals that the maximum wavelength shifts caused by alcohol and distilled water are −10.5 and −12.5 pm, respectively. It should be noted that the resonance wavelength variation of alcohol is contributed by droplet gravity and heat dissipation, due to the endothermic nature of alcohol evaporation, even though the wavelength shift induced by alcohol is still smaller than that by distilled water due to the significant difference in maximum droplet gravity. As such, alcohol and distilled water identification could be achieved according to the difference between detached time and maximum wavelength shift.

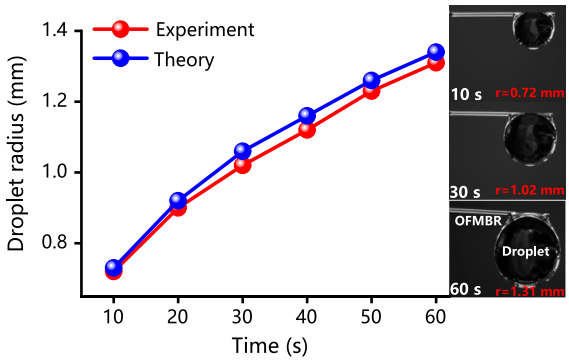

Fig. 7. Comparison of pendant droplet radius between experiment (red dots) and theoretical (blue dots) values. Right side shows images of pendant droplet of distilled water at different moments.

To observe the morphology of pendant droplets with a micrometer to millimeter scale radius, a CCD camera is employed to monitor the pendant droplet formation. The morphologies of the distilled water pendant droplet as time evolves are shown on the right side of Fig. 7, which present a sphere under microgravity, and a slight deformation occurs as the radius increases to millimeter-scale [5]. Furthermore, the radius of the pendant droplets can be deduced by converting the measured pixel length to the actual value. Figure 7 shows the comparison of pendant droplet radius between experimental and theoretical values, which are calculated based on Eq. (1). The experimental results are in agreement with the theoretical ones, where the little difference can be ascribed to the liquid evaporation [17] and limited pixel and resolution of the CCD camera.

4. CONCLUSION

We have proposed and demonstrated a liquid mass and liquid type identification sensor, utilizing a tapered fiber and an OFMBR. Theoretically, the influence of droplet gravity on device displacement is analyzed using COMSOL simulation software. It reveals that droplet gravity contributes to altering the coupling states between tapered fiber and OFMBR, which shifts the resonance wavelength. Experimentally, we first verify that the proposed sensor works with periodicity; then, the liquid mass sensing experiment is carried out. The maximum sensitivity of −3.34 pm/mg is obtained at the flow rate of 10 μL/min. Moreover, the distilled water and alcohol are identified due to their distinguished surface tension coefficients, and the morphologic variation of pendant droplet is monitored under CCD camera. Our sensor provides a scheme to characterize the liquid properties, which has enormous potential in droplet generation and identification-related microfluidic applications.

Funding. National Natural Science Foundation of China (61875116, 62022053); Open Project Program of Wuhan National Laboratory for Optoelectronics (2018WNLOKF014); 111 Project (D20031); Advanced Optical Waveguide

Intelligent Manufacturing and Testing Professional Technical Service Platform of Shanghai (19DZ2294000).

Disclosures. The authors declare no conflicts of interest.

Data Availability. Data underlying the results presented in this paper are not publicly available at this time but may be obtained from the authors upon reasonable request.

REFERENCES

1. P. J. Galley and G. M. Hieftje, "Technique for producing capillaries with reproducible orifice diameters for uniform droplet generation," Appl. Spectrosc. **46**, 1460–1463 (1992).
2. Y. C. Tan, J. S. Fisher, A. I. Lee, V. Cristini, and A. P. Lee, "Design of microfluidic channel geometries for the control of droplet volume, chemical concentration, and sorting," Lab Chip **4**, 292–298 (2004).
3. S. Daniel, M. K. Chaudhury, and J. C. Chen, "Fast drop movements resulting from the phase change on a gradient surface," Science **291**, 633–636 (2001).
4. E. Preter, R. A. Katims, V. Artel, C. N. Sukenik, D. Donlagic, and A. Zadok, "Monitoring and analysis of pendant droplets evaporation using bare and monolayer-coated optical fiber facets," Opt. Mater. Express **4**, 903–915 (2014).
5. Q. M. Lv, Y. C. Wu, C. Li, X. C. Wu, L. H. Chen, and K. F. Cen, "Surface tension and viscosity measurement of oscillating droplet using rainbow refractometry," Opt. Lett. **45**, 6687–6690 (2020).
6. X. G. Li, R. X. Wang, H. X. Shi, and B. H. Song, "Effective surface tension of liquid marbles using controllable nanoparticle monolayers," Appl. Phys. Lett. **113**, 101602 (2018).
7. A. Giorgini, S. Avino, P. Malara, P. D. Natale, and G. Gagliardi, "Opto-mechanical oscillator in a nanoliter droplet," Opt. Lett. **43**, 3473–3477 (2018).
8. R. Lee, P. Zhang, Y. Xu, and S. Jung, "Radiation pressure-induced nonlinearity in a micro-droplet," Opt. Express **28**, 12675–12682 (2020).
9. S. Maayani and T. Carmon, "Droplet Raman laser coupled to a standard fiber," Photon. Res. **7**, 1188–1192 (2019).
10. D. D. Ambrosio, M. Capezzuto, S. Avino, P. Malara, A. Giorgini, P. D. Natale, and G. Gagliardi, "Light pressure in droplet micro-resonators excited by free-space scattering," Opt. Lett. **46**, 3111–3114 (2021).
11. S. Maayani, L. L. Martin, S. Kaminski, and T. Carmom, "Cavity opto-capillaries," Optica **3**, 552–555 (2015).
12. A. Jonas, Y. Karadag, M. Mestre, and A. Kiraz, "Probing of ultrahigh optical Q-factors of individual liquid microdroplets on superhydrophobic surfaces using tapered optical fiber waveguides," J. Opt. Soc. Am. B **29**, 3240–3247 (2012).
13. M. Ivanov, K. Chang, I. Galinskiy, B. Mehlig, and D. Hanstorp, "Optical manipulation for studies of collisional dynamics of micron-sized droplets under gravity," Opt. Express **25**, 1391–1404 (2017).
14. S. Kaminske, L. L. Martin, and T. Carmom, "Tweezers controlled resonator," Opt. Express **23**, 28914–28919 (2015).
15. S. Zhu, Y. Liu, L. Shi, X. Xu, and X. Zhang, "Extinction ratio and resonant wavelength tuning using three dimensions of silica microresonators," Photon. Res. **4**, 191–196 (2016).
16. H. Wan, J. Chen, C. Wan, Q. Zhou, J. Wang, and Z. Zhang, "Optofluidic microcapillary biosensor for label-free, low glucose concentration detection," Biomed. Opt. Express **10**, 3929–3937 (2019).
17. T. Hamidfar, K. V. Tokmakov, B. J. Mangan, R. S. Windeler, A. V. Dmitriev, D. L. P. Vitullo, P. Bianucci, and M. Sumetsky, "Localization of light in an optical microcapillary introduced by a droplet," Optica **5**, 382–388 (2018).
18. K. Han, J. H. Kim, and G. Bahl, "High-throughput sensing of freely flowing particles with optomechanofluidics," Optica **3**, 585–591 (2016).
19. F. Xie, N. Yao, W. Fang, H. Wang, F. Gu, and S. Zhuang, "Single-mode lasing via loss engineering in fiber-taper-coupled polymer bottle microresonators," Photon. Res. **5**, B29–B33 (2017).
20. Y. Louyer, D. Mechede, and A. Rauschenbeutel, "Tunable whispering gallery mode resonators for cavity quantum electrodynamics," Phys. Rev. A **72**, 2409–2413 (2005).
21. H. Y. Li, B. Sun, Y. G. Yuan, and J. Yang, "Guanidine derivative polymer coated microbubble resonator for high sensitivity detection of CO_2 gas concentration," Opt. Express **27**, 1991–2000 (2019).
22. Z. D. Peng, C. Q. Yu, H. L. Ren, C. L. Zou, G. C. Guo, and C. H. Dong, "Gas identification in high-*Q* microbubble resonators," Opt. Lett. **45**, 4440–4443 (2020).
23. F. Y. Hou, X. B. Zhang, L. Yang, W. Sun, Y. Yang, Y. H. Dong, Y. Huang, and T. Y. Wang, "Magnetic fluid infiltrated microbottle resonator sensor with axial confined mode," IEEE Photon. J. **12**, 6802709 (2020).
24. L. Hao and X. D. Fan, "Characterization of sensing capability of optofluidic ring resonator biosensors," Appl. Phys. Lett. **97**, 011105 (2010).
25. Z. H. Guo, Q. J. Liu, C. G. Zhu, B. W. Wang, Y. Zhou, and X. Wu, "Ultra-sensitive biomolecular detection by external referencing optofluidic microbubble resonators," Opt. Express **27**, 12424–12435 (2019).
26. J. S. Pan, B. Zhang, Z. Y. Liu, J. X. Zhao, Y. H. Feng, L. Wan, and Z. H. Li, "Microbubble resonators combined with digital optical frequency comb for high-precision air-coupled ultrasound detectors," Photon. Res. **8**, 303–310 (2020).
27. J. M. Ward, Y. Yang, F. C. Lei, X. C. Yu, Y. F. Xiao, and S. N. Chormaic, "Nanoparticle sensing beyond evanescent field interaction with a quasi-droplet microcavity," Optica **5**, 674–677 (2018).
28. W. Chen, J. Zhang, B. Peng, Ş. K. Özdemir, X. Fan, and L. Yang, "Parity-time-symmetric whispering-gallery mode nanoparticle sensor," Photon. Res. **6**, A23–A30 (2018).
29. D. Q. Yang, F. Gao, Q. T. Cao, C. Wang, Y. F. Ji, and Y. F. Xiao, "Single nanoparticle trapping based on on-chip nanoslotted nanobeam cavities," Photon. Res. **6**, 99–108 (2018).
30. D. Q. Yang, A. Q. Wang, J. H. Chen, X. C. Yu, C. W. Lan, Y. F. Ji, and Y. F. Xiao, "Real-time monitoring of hydrogel phase transition in an ultrahigh *Q* microbubble resonator," Photon. Res. **8**, 497–502 (2020).
31. D. Q. Yang, J. H. Chen, Q. T. Cao, B. Duan, H. J. Chen, X. C. Yu, and Y. F. Xiao, "Operando monitoring transition dynamics of responsive polymer using optofluidic microcavities," Light Sci. Appl. **10**, 128 (2021).
32. Z. J. Wang, X. B. Zhang, S. C. Zhao, Y. Yu, H. Sun, Y. Yang, Y. H. Dong, Y. Huang, and T. Y. Wang, "High sensitivity flow rate sensor enabled by higher order modes of packaged microbottle resonator," IEEE Photon. Technol. Lett. **33**, 599–603 (2021).
33. Z. M. Chen, Z. H. Guo, X. Mu, Q. Li, X. Wu, and H. Y. Fu, "Packaged microbubble resonator optofluidic flow rate sensor based on Bernoulli Effect," Opt. Express **27**, 36932–36940 (2019).
34. T. Loppolo, U. K. Ayaz, and M. V. Otugen, "High-resolution force sensor based on morphology dependent optical resonances of polymeric spheres," J. Appl. Phys. **105**, 013535 (2009).
35. L. E. Malvern, *Introduction to the Mechanics of a Continuous Medium* (Prentice Hall, 1969).
36. M. E. Gurtin, *The Linear Theory of Elasticity* (Springer, 1973).
37. B. T. Cao, "Solutions of Navier equations and their representation structure," Adv. Appl. Math. **43**, 331–374 (2009).
38. J. M. Ward, Y. Yang, and S. N. Chormaic, "Glass-on-glass fabrication of bottle-shaped tunable microlasers and their applications," Sci. Rep. **6**, 25152 (2015).